

PartSDF: Part-Based Implicit Neural Representation for Composite 3D Shape Parametrization and Optimization

Nicolas Talabot¹ Olivier Clerc¹ Arda Cinar Demirtas² Doruk Oner² Pascal Fua¹

Abstract

Accurate 3D shape representation is essential in engineering applications such as design, optimization, and simulation. In practice, engineering workflows require structured, part-aware representations, as objects are inherently designed as assemblies of distinct components. However, most existing methods either model shapes holistically or decompose them without predefined part structures, limiting their applicability in real-world design tasks. We propose PartSDF, a supervised implicit representation framework that explicitly models composite shapes with independent, controllable parts while maintaining shape consistency. Despite its simple single-decoder architecture, PartSDF outperforms both supervised and unsupervised baselines in reconstruction and generation tasks. We further demonstrate its effectiveness as a structured shape prior for engineering applications, enabling precise control over individual components while preserving overall coherence. Code available at <https://github.com/cvlab-epfl/PartSDF>.

1. Introduction

We live in a world full of manufactured objects of ever-increasing complexity that require clever engineering to be functional. These objects are inherently composite. Thus Computer Aided Design (CAD) tools used to design and optimize them must be able to handle them as assemblies of distinct parts from the outset. Each part must adhere to separate fabrication constraints, tolerances, and functional requirements, making part-based representations essential. Unlike in many publicly available 3D datasets where shapes are treated as holistic entities, real-world engineering applications therefore require structured, part-aware models to support tasks such as simulation, optimization, and interactive design refinement. For example, when optimizing

¹EPFL, Lausanne, Switzerland ²Bilkent University, Ankara, Türkiye. Correspondence to: Nicolas Talabot, Pascal Fua <first.last@epfl.ch>.

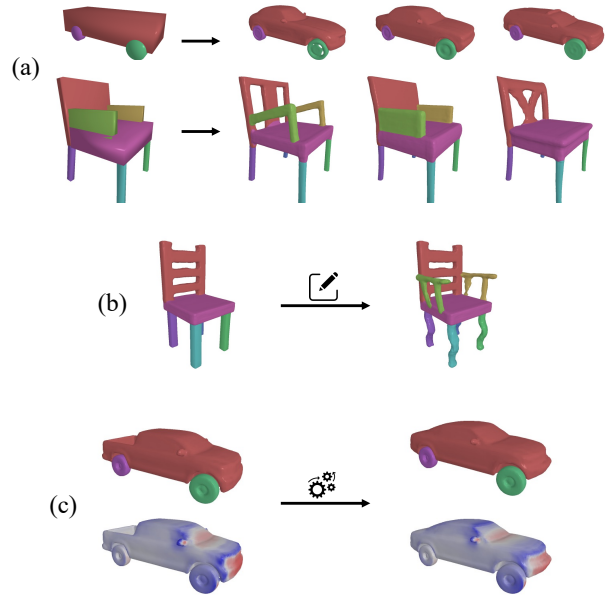


Figure 1. Part-based implicit representation. PartSDF is a modular approach to representing composite 3D shapes for a variety of purposes thanks to the simplicity of our part decoder: (a) shape generation, optionally conditioned on part layouts, and *part-based* (b) manipulation and (c) optimization. (c) The car body (in red) is optimized to reduce aerodynamic drag, without editing the wheels.

the aerodynamics of a car, correctly identifying wheels is crucial for defining appropriate boundary conditions and to ensure that they stay separate from the body.

With these requirements in mind, implicit Neural Representations (INRs) (Park et al., 2019; Mescheder et al., 2019; Chen & Zhang, 2019) have become a well-established approach to providing smooth and topology-agnostic models. However, most INR-based methods employ global shape representations, making them unsuitable for these purposes. Recent INR works have explored learning part decompositions (O. et al., 2022; Chen et al., 2023), but unsupervised methods often struggle with consistency and semantic coherence—critical aspects in engineering workflows where part definitions are predefined and must remain stable across designs. Even supervised approaches (Wu et al., 2020; Deng et al., 2022; Li et al., 2024) primarily focus on generation or manipulation rather than providing a structured shape prior

that enables controlled modifications or optimizations while preserving inter-part relationships.

To address these limitations, we introduce PartSDF, a supervised, part-aware implicit representation designed for composite shapes. Our approach explicitly encodes each part with a latent vector and pose parameters, ensuring independent control while maintaining global consistency. Unlike prior works that rely on complex architectures (Deng et al., 2022; O. et al., 2022; Li et al., 2024), PartSDF achieves excellent results with a simpler decoder architecture. This formulation makes it particularly effective for shape reconstruction, generation, optimization, and targeted manipulation—key requirements in engineering applications.

Our auto-decoding framework learns a structured shape prior, which can be leveraged by secondary models for various tasks. Additionally, we introduce a novel strategy for supervising parts without assuming watertight segmentation, using the global shape’s signed distance field (SDF). Each part’s SDF is an explicit output, enabling the enforcement of topological constraints during training—an aspect that, while not the primary focus of this work, may be explored in the future.

Our main contributions are as follows:

- We introduce a supervised, part-aware implicit representation that models each component independently, ensuring both expressiveness and part consistency.
- We demonstrate that our approach serves as a versatile basis for various tasks such as shape reconstruction, optimization, and manipulation, all with the same core decoder network.
- We propose a novel part supervision technique relying on the full shape’s SDF and inter-part losses, applicable to both watertight and non-watertight segmentations.

Through comprehensive evaluations, we show that PartSDF effectively captures the structure of composite shapes, making it well-suited for engineering applications where part-aware control is essential.

2. Related Work

Over the last several decades, the evolution of traditional CAD systems has reflected a fundamental tension between simplicity and expressiveness. Early approaches relied on basic geometric primitives such as spheres, cylinders, and NURBS surfaces (Piegl, 1991), offering mathematical precision but limited representational power. Recent years have witnessed a shift toward more sophisticated primitives, from simple cuboids (Tulsiani et al., 2017; Niu et al., 2018; Sun et al., 2019; Kluger et al., 2021) to learned deep representation, which we briefly review here. We start with generic 3D shape representations learned from data and continue

with more-flexible part-based approaches.

2.1. Learned 3D Shape Representation

Learning-based methods for 3D shape representation have evolved significantly, beginning with explicit approaches such as voxel grids, point clouds, and meshes. Voxel-based methods (Wu et al., 2015; 2016; Choy et al., 2016; Dai et al., 2017) partition 3D space into grids, but are memory-intensive at finer resolutions, which can be mitigated using octrees (Riegler et al., 2017; Tatarchenko et al., 2017), but only up to a point. Point clouds reduce memory costs by representing shapes as surface points but ignore connectivity, which can compromise topological consistency (Fan et al., 2017; Yang et al., 2018; Achlioptas et al., 2018; Peng et al., 2021; Zeng et al., 2022). Meshes, though well-suited for detailed surface representation, impose a rigid topology that is difficult to modify (Groueix et al., 2018; Kanazawa et al., 2018; Wang et al., 2018; Pan & Jia, 2019).

Implicit Neural Representations (INRs) offer a flexible alternative, defining shapes as continuous functions of the 3D space that encode the surface implicitly (Park et al., 2019; Mescheder et al., 2019; Chen & Zhang, 2019; Xu et al., 2019). It can then be recovered explicitly using meshing algorithms (Lorensen & Cline, 1987; Lewiner et al., 2003; Ju et al., 2002). Even though these meshing algorithms may not be themselves differentiable, differentiability can be preserved by relying on the implicit function theorem (Guillard et al., 2024), enabling back-propagation from the explicit surface, for example when optimizing a shape to maximize its aerodynamic performance (Baque et al., 2018). Extensions enable shape manipulation (Hao et al., 2020), point-cloud reconstruction (Peng et al., 2020), and training directly from point data (Atzmon & Lipman, 2020; Gropp et al., 2020). Newer works (Sitzmann et al., 2020; Takikawa et al., 2021) improve the accuracy further with new latent representations, such as irregular grids (Zhang et al., 2022) or unordered sets (Zhang et al., 2023).

2.2. Part Based Models

As effective as they are, the INRs described above model 3D shapes as single entities, limiting their capacity to represent structured, part-based composite objects. This requires decomposing the shapes into their component parts, which can be done in a supervised or unsupervised manner.

Unsupervised Part Decomposition. Early unsupervised approaches learn shape abstractions using local primitives such as cuboids (Tulsiani et al., 2017; Zou et al., 2017; Sun et al., 2019; Smirnov et al., 2020; Yang & Chen, 2021), superquadrics (Paschalidou et al., 2019; 2020), anisotropic Gaussians (Genova et al., 2019), or convexes (Deng et al., 2020), approximating complex shapes as combinations of simpler parts. More recently, complex objects are better rep-

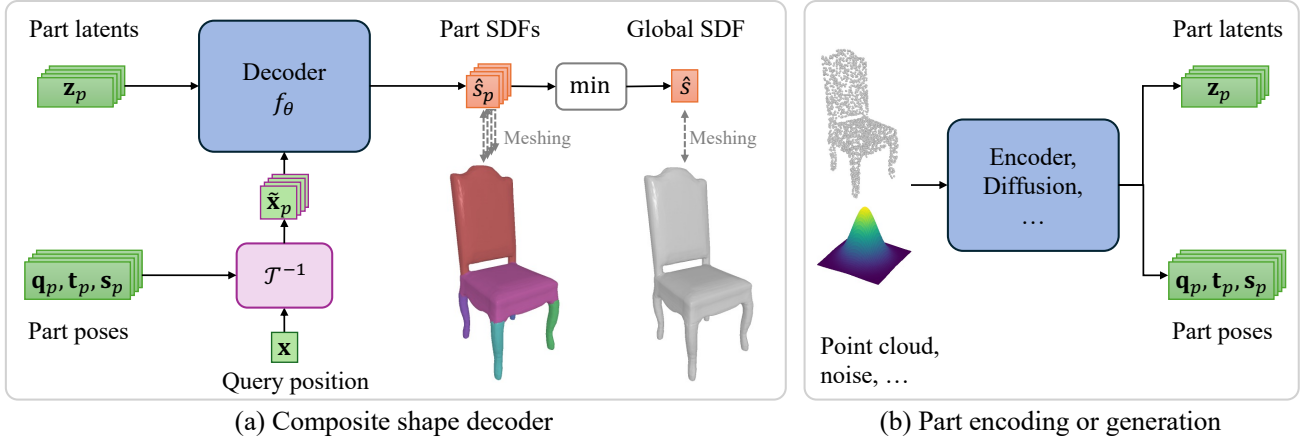


Figure 2. **PartSDF pipeline.** (a) Our model’s core is a part auto-decoder f_θ that takes as input part latents \mathbf{z}_p and poses expressed in terms of a quaternion \mathbf{q}_p , translation \mathbf{t}_p , and scale s_p , along with the query position $\mathbf{x} \in \mathbb{R}^3$. It outputs signed distances \hat{s}_p for all parts at the queried position, which may be combined into the global signed distance. (b) A secondary model may be used based on the task at hand, such as encoders to map a given modality, e.g., point clouds, to part latents and poses, or a diffusion model to generate them from noise.

represented by predicting and deforming primitives (Paschali-dou et al., 2021; Shuai et al., 2023), creating deformable part templates (Hui et al., 2022; Chen et al., 2023), or performing part-based co-segmentation, which consistently divides shapes into parts across a dataset without relying on labeled boundaries (O. et al., 2022) or does so for only a subset of the data (Chen et al., 2019). For shape manipulation, SPAGHETTI (O. et al., 2022) utilizes a transformer to predict Gaussian parts from a global latent vector and reconstructs them into a single cohesive object. This approach supports interactive editing of user-defined parts and can be combined with SALAD (Koo et al., 2023), which employs a cascaded diffusion model for part generation. However, the parts learned by these methods are typically arbitrary and lack semantic meaning, making them unsuitable for tasks requiring specific, predefined part structures.

Supervised Part Representation. Supervised methods leverage known part decompositions to create explicit, structured representations of composite shapes. HybridSDF (Vasu et al., 2022) mixes INRs with geometric primitives to represent and manipulate shapes, while ANISE (Petrov et al., 2023) learns to assemble implicit parts for reconstruction from images and point clouds. Instead, ProGRIP (Deng et al., 2022), PQ-NET (Wu et al., 2020), and PASTA (Li et al., 2024) focus on composite shape generation. ProGRIP relies on shape programs to produce composite INR shapes, while PQ-NET uses a GRU-based RNN (Cho et al., 2014) as an auto-encoder for sequences of parts, with latentGANs (Achlioptas et al., 2018) for generation. PASTA employs an auto-regressive transformer to predict part bounding boxes that are decoded into a single global shape, similarly to SPAGHETTI.

While effective for shape generation, these supervised methods forgo part consistency across shapes and continuous

shape parametrization. Thus, there is a need for an approach that leverages part supervision to produce modular, flexible representations that can output composite shapes by parts and act as part and shape priors in backward tasks such as optimization. PartSDF aims to fulfill that need.

3. Method

We propose PartSDF, a modular, part-based representation for composite shapes, designed for flexibility across applications that require both structured part manipulation and optimization. Given a dataset of composite shapes with known part decompositions, our model learns to represent each one independently within a compact latent space, while being able to maintain consistency when deforming them.

As shown in Figure 2, our framework consists of two primary components. First, the core of our model is a *composite shape decoder* that outputs a signed distance function (SDF) for each part, parameterized by a latent vector and a pose (Section 3.1). It is trained in an auto-decoding fashion (Park et al., 2019) in which the latent vectors and the decoder’s weights are learned simultaneously, with supervision applied at both the global and part levels (Section 3.2). Second, our architecture supports secondary models for *part encoding or generation*, allowing further adaptation of part latents and poses for tasks such as shape reconstruction or generation, while maintaining the same core part decoder for efficient inference and manipulation (Section 3.3).

3.1. Composite Shape Decoder

In our composite shape representation, shown in Figure 2(a), each part is described by a latent vector $\mathbf{z}_p \in \mathbb{R}^Z$ and a pose $\mathbf{p}_p \in \mathbb{R}^{10}$, consisting of a rotation quaternion $\mathbf{q}_p \in \mathbb{R}^4$,

translation $\mathbf{t}_p \in \mathbb{R}^3$, and scale $s_p \in \mathbb{R}^3$. Given a query point $\mathbf{x} \in \mathbb{R}^3$, each part’s pose maps the query point into the part’s canonical space via inverse transformation \mathcal{T}^{-1} , resulting in the transformed query point $\hat{\mathbf{x}}_p = \mathcal{T}^{-1}(\mathbf{x}, \mathbf{p}_p)$, $\forall p$. The decoder f then outputs the SDF for each part at this transformed point

$$\hat{s}_p = f(\mathbf{z}_p, \hat{\mathbf{x}}_p). \quad (1)$$

The SDFs for all parts can then be combined to recover the full shape representation as $\hat{s} = \min_p \hat{s}_p$.

In PartSDF, the decoder f is implemented as a multi-layer perceptron (MLP) with modifications to support part-based representation. First, we perform *latent modulation* (Dupont et al., 2022) by injecting the part latent vectors \mathbf{z}_p at every fully-connected layer of the MLP. Then, we introduce a per-part learnable bias into these layers to help differentiate the individual parts. We formalize these layers h_{fc} as

$$\mathbf{x}_p^{l+1} = h_{fc}^l(\mathbf{z}_p, \mathbf{x}_p^l) = \sigma(\mathbf{W}^l \mathbf{x}_p^l + \mathbf{b}^l + \mathbf{W}_z^l \mathbf{z}_p + \mathbf{b}_p^l), \quad (2)$$

where σ is an activation function, \mathbf{x}_p^l denotes the features of part p at layer l , $(\mathbf{W}^l, \mathbf{b}^l)$ are the layer’s parameters, \mathbf{W}_z^l is the parameters of the *latent modulation*, and \mathbf{b}_p^l the learnable bias of part p at layer l .

This creates a part-specific MLP structure with extensive weight sharing across parts. However, it processes each part independently, which is not desirable if they are to adapt to each others when the composite shape is manipulated. To remedy this, we incorporate 1D convolutions with a kernel size of 1 between each h_{fc} layer. These convolutions operate across parts, treating them as the “channel” dimension, with one filter \mathbf{w}_p per part. Hence, for each feature dimension d :

$$\mathbf{x}_p^{l+1}[d] = \sigma\left(\sum_{i=1}^P \mathbf{w}_p^l[i] \cdot \mathbf{x}_i^l[d] + b_p^l\right), \forall p, d. \quad (3)$$

Conceptually, they function as the h_{fc} layers, but on another input dimension: They process all parts for each feature individually (see Appendix B.1 for a visualization). This enables the decoder to capture inter-part dependencies and improve adaptability during part manipulation, as shown in our ablation study (Appendix E). Our final model f_θ , with θ containing all trainable parameters, operates on all parts. We write

$$\hat{s} = f_\theta(\mathbf{Z}, \hat{\mathbf{X}}), \quad (4)$$

where \hat{s} , \mathbf{Z} , and $\hat{\mathbf{X}}$ are all parts’ SDF, latents, and transformed query points respectively.

3.2. Training

Let us consider a dataset \mathcal{D} where each shape \mathcal{S} is decomposed in up to P parts, given as the segmentation of its surface. To establish initial poses for each part, we fit simple primitives—cuboids or cylinders—to the segmented

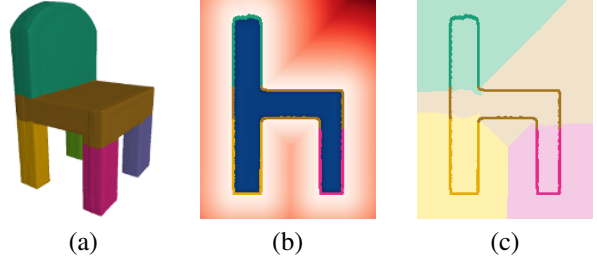


Figure 3. **Non-watertight part supervision strategy.** (a) Part decomposition of a chair, (b) a 2D slice of its signed distances (red/blue) with parts highlighted in color, and (c) the specific regions of spaces in where each part is supervised.

parts and use these primitives’ poses as the part poses. Therefore, each element of the dataset becomes a tuple $\mathcal{D} = \{(\mathcal{S}, \{\mathcal{P}_p\}, \{\mathbf{p}_p\})_i\}$ of the shape, its parts, and their poses, where we write $\mathbf{p}_p = (\mathbf{q}_p, \mathbf{t}_p, s_p)$.

Training the Decoder. For watertight shapes \mathcal{S} , PartSDF’s decoder is then trained in an auto-decoding fashion (Park et al., 2019), where model parameters θ and part latent vectors \mathbf{z}_p are optimized jointly. Note that we can directly use the parts poses from \mathcal{D} during training. When a part is missing from a specific shape, we assign it the average pose of that part over the dataset, allowing the model to naturally learn to output $\text{SDF} > 0$ for nonexistent parts, without having to predict an *existence score*, as in (Petrov et al., 2023).

Some parts \mathcal{P}_p , however, may *not* be watertight as they are a subset of \mathcal{S} ’s surface that may not be closed. Rather than computing an approximate SDF or editing the parts to make them watertight (Wu et al., 2020; Petrov et al., 2023), we adopt a different supervision strategy. Each part is supervised using the full shape’s SDF, but only in the region of space where each 3D point is closest to this part and not the other. Formally, a part \mathcal{P}_p is supervised in $\{\mathbf{x} \in \mathbb{R}^3 \mid p = \arg \min_i d_i(\mathbf{x})\}$, where $d_i(\mathbf{x})$ is the projection distance of \mathbf{x} to part i , as depicted by Figure 3. To further prevent overlaps, we incorporate a non-intersection loss that maintains spatial separation between parts.

Loss Function. For any shape from \mathcal{D} , we minimize

$$\mathcal{L} = \mathcal{L}_{\text{sdf}} + \mathcal{L}_{\text{part}} + \mathcal{L}_{\text{inter}} + \lambda \sum_p \|\mathbf{z}_p\|^2, \quad (5)$$

where λ is a hyperparameter controlling the latent L_2 -regularization and the loss terms are defined below.

For the whole shape, we minimize

$$\mathcal{L}_{\text{sdf}} = \frac{1}{|\mathcal{X}|} \sum_{(\mathbf{x}_i, s_i) \in \mathcal{X}} |\hat{s} - s_i|, \quad (6)$$

where \mathcal{X} is a set of sampled points in 3D and around \mathcal{S} , with their ground truth SDF s_i from the full shape \mathcal{S} . \hat{s} is

the predicted SDF at those points. For notational simplicity, we omit the dependency on θ and the \mathbf{z}_p along with the clamping of SDF values (Park et al., 2019).

For individual parts, we minimize

$$\mathcal{L}_{\text{part}} = \frac{1}{|\mathcal{X}|} \sum_{(\mathbf{x}_i, s_i, p_i) \in \mathcal{X}} |\hat{s}_{p_i} - s_i|, \quad (7)$$

with an additional index p_i of the part closest to \mathbf{x}_i , re-using \mathcal{X} as a slight abuse of notation to explicit that we compute these losses on the same 3D samples. \hat{s}_{p_i} is the predicted part SDF at those points.

Finally, we introduce a non-intersection loss that pushes the SDF of parts to be positive at each position \mathbf{x}_i where at least two parts have $\text{SDF} < 0$. Using $\hat{\mathcal{X}}$ as the subset of such 3D points, the loss is written

$$\mathcal{L}_{\text{inter}} = \frac{1}{|\hat{\mathcal{X}}|} \sum_{\mathbf{x}_i \in \hat{\mathcal{X}}} |\mathbf{w}_i \cdot \hat{\mathbf{s}}_i|, \quad (8)$$

where $\hat{\mathbf{s}}_i$ is the vector of predicted part SDF at point \mathbf{x}_i and $\mathbf{w}_i = \text{softmax}(\tilde{\mathbf{s}}_i)$, defining $\tilde{\mathbf{s}}_i$ as $\hat{\mathbf{s}}_i$ with all positive values replaced by $-\infty$. These weights pushes predicted SDFs that are closer to 0, more strongly towards > 0 .

3.3. Part Encoding and Generation

Once PartSDF’s decoder is trained, it is frozen to be used for downstream tasks, optionally in conjunction with separate specialized networks. While this requires training two networks independently, it makes the training of each one easier. Furthermore, the decoder need only been trained once and used again and again for the different tasks.

Encoding To reconstruct a shape from a given modality, *e.g.*, point clouds or images, encoders can be trained to directly predict part latents and poses, to then be decoded with PartSDF: with input data \mathcal{I} corresponding to the shape of our training data \mathcal{D} , encoders are trained to map this new modality to the part latents and poses of our pre-trained decoder. As an example, we show how to reconstruct unseen shapes for which part decomposition is unknown in Section 4.1. We do this by training a point cloud encoder to predict part latents and poses, which are then refined in an auto-decoding strategy and part-agnostic manner.

Generation For shape generation with a coherent part set, generative models can be trained to map random noise to the parts parametrization. Generative Adversarial Networks (GAN) (Goodfellow et al., 2014) have been used to generate shape latents, often dubbed *latentGANs* in related work (Achlioptas et al., 2018; Chen & Zhang, 2019) such as PQ-NET (Wu et al., 2020). Recently, diffusion models (Sohl-Dickstein et al., 2015; Ho et al., 2020) have gained

a lot of traction for their generative performances, even in shape (Zhang et al., 2023) or part-based generation (Koo et al., 2023). Generating new shapes with PartSDF can then be achieved by training such generative models on the part poses and latents of our pre-trained encoder and, even if not shown here, could be extended to conditional generation on images or texts (Zhang et al., 2023; Koo et al., 2023).

4. Experiments

In this section, we demonstrate how our method can be applied to various tasks and compare it to several part-based baselines. Further experimental details and additional results are available in Appendix B and F, respectively.

Datasets Obtaining high-quality composite shape data is challenging as many detailed datasets tend to remain private. Public datasets, such as ShapeNet (Chang et al., 2015) and PartNet (Mo et al., 2019), often suffer from over-segmentation and inconsistencies in part definitions across samples, or provide only coarse semantic segmentations that lack the granularity needed for precise part manipulation. To remedy this, we use three curated datasets that offer consistent and well-defined part decompositions: (1) *Car*, a hand-processed subset of ShapeNet in which the wheels of the cars are separated from the main body; (2) *Mixer*, a set of liquid mixers made of a central helix within a tube and two attach points (Vasu et al., 2022); and (3) *Chair*, a cleaned subset of ShapeNet chairs, segmented with PartNet’s semantic labels and further divided into individual legs and arms. There are 1046, 1949, and 1332 shapes in each dataset with 5, 4, and 8 parts, respectively. We use 80% of the data for training and the remaining 20% as the unseen test set.

Baselines. For part-based baselines, we have unfortunately found no publicly available code for modern architectures such as ProGRIP (Deng et al., 2022), SPAGHETTI (O. et al., 2022) and PASTA (Li et al., 2024). We therefore use DAE-NET (Chen et al., 2023) that learns deformable part template in an *unsupervised* manner, BAE-NET (Chen et al., 2019) that uses *weak supervision* with 8 labeled shapes, and PQ-NET (Wu et al., 2020), a *fully-supervised* approach that supports shape generation. As these part-based baselines are several years old, we also compare against the state-of-the-art 3DShape2VecSet, or 3DS2VS for short (Zhang et al., 2023). It is not ideal because, not being part-based, it is not suitable for engineering design. However, it gives an upper bound on the accuracy that can currently be obtained if one ignores the part decomposition, which typically allows for higher precision than when enforcing it.

Metrics. Reconstruction accuracy is assessed using three different metrics: Chamfer-Distance (CD) for surface accuracy, Intersection over Union (IoU) for volume, and Image Consistency (IC) (Guillard et al., 2022) for shape appear-

Table 1. **Shape reconstruction.** We compute the average Chamfer-Distance CD ($\times 10^4$), Intersection over Union IoU (%), and Image Consistency IC between reconstructions and corresponding test shapes. We also report average per-part Intersection over Union pIoU (%) for part-based methods. Ours-1P uses a single part to reconstruct the full shape and Ours-PC uses a point cloud encoder to get initial part latents and poses that are refined in a part-agnostic manner.

	CD (\downarrow)			IoU (% , \uparrow)			IC (\uparrow)			pIoU (% , \uparrow)		
	Car	Mixer	Chair	Car	Mixer	Chair	Car	Mixer	Chair	Car	Mixer	Chair
3DShape2VecSet	2.79	25.35	4.03	92.86	61.85	91.48	0.896	0.830	0.898	-	-	-
Ours-1P	1.37	1.44	3.74	97.41	95.16	93.78	0.924	0.978	0.913	-	-	-
DAE-NET	28.38	15.93	100.49	81.91	70.14	56.37	0.797	0.918	0.662	34.71	31.83	52.80
BAE-NET	33.43	13.68	106.60	75.17	33.38	40.79	0.771	0.818	0.594	21.83	31.14	38.72
PQ-NET	30.20	17.75	38.90	72.00	26.71	49.09	0.754	0.739	0.690	36.27	25.67	51.48
Ours	1.27	1.60	1.27	98.02	94.43	97.19	0.931	0.978	0.943	94.89	90.42	91.40
Ours-PC	1.28	1.73	1.30	97.95	83.38	97.04	0.930	0.966	0.941	94.25	78.61	87.42

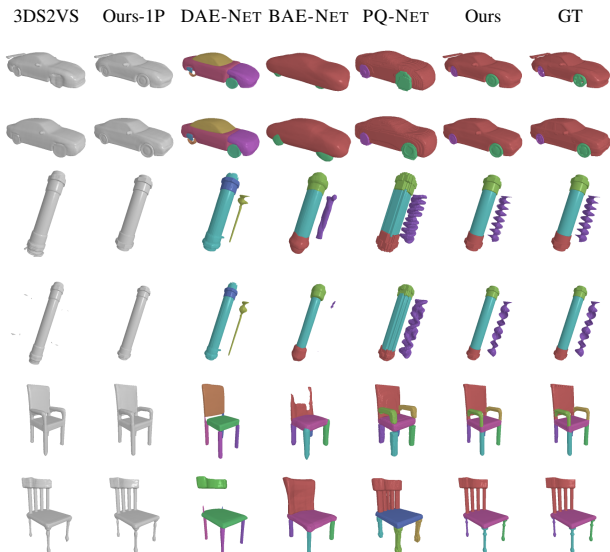


Figure 4. **Shape reconstruction.** Reconstruction of test shapes with all models. For part-based method, we color each part with a different color and translate the helix outside of the mixers for visualization. Best viewed digitally.

ance and normals. Part reconstruction is evaluated by averaging the per-part IoU and, as we do not make the assumption that parts must be watertight, we compute part occupancies using the same strategy as for our training losses in Section 3.2. For generation, we report Minimum Matching Distance (MMD) and Coverage Score (COV) (Achlioptas et al., 2018), using CD as the distance metric.

4.1. Shape and Part Reconstruction

We evaluate the accuracy of shape and part reconstruction across all datasets and methods. To encode new test shapes at inference time, our model relies on auto-decoding: It remains frozen while reconstruction losses are minimized with respect to the latent vectors. We also report results for

PartSDF with a single part, *i.e.*, using our decoder in a part-agnostic manner, and refer to it as Ours-1P. We reconstruct meshes using Marching Cubes (Lorensen & Cline, 1987; Lewiner et al., 2003) at a resolution of 256 for all methods. We report quantitative results in Table 1, with qualitative ones shown in Figure 4. Across all metrics, our method achieves the best results on cars and chairs, and equivalent results on mixers to Ours-1P, which does not reconstruct individual parts. We note that 3DShape2VecSet particularly struggles on this data, creating spurious floating surfaces and missing the central helices. Other part-based methods fall significantly behind on both surface and volume metrics.

One thing that handicaps part-aware baselines is their reliance on voxelized data despite being INR-based: For speed and memory, the data is binarized and voxelized at 64^3 , which delivers efficient and fast models but greatly limits accuracy. This is particularly visible in the case of the thin helix of the mixers or the equally thin chair parts: They tend to either disappear or be inflated. Instead, PartSDF is trained with samples directly obtained from the original shape \mathcal{S} and yields superior accuracy, capturing detailed part-specific geometry and structure. It is likely that approaches relying on more complex architectures (Deng et al., 2022; O. et al., 2022; Li et al., 2024) would be more competitive in reconstruction accuracy. However, as discussed in Section 2, they are not designed to provide composite shape priors usable for tasks such as part-based optimization.

To illustrate that part encoder models can be used in conjunction with PartSDF, we also reconstruct the test set in a part agnostic manner: We encode each shape’s surface point cloud to obtain initial latents and poses, which are then refined with our auto-decoding strategy but *without* $\mathcal{L}_{\text{part}}$. As encoder, we use 3DShape2VecSet of reduced size, without the final cross-attention and, to produce an *ordered* set of latents and poses, learnable queries at the shape encoding level. As can be seen in the last row of Table 1, this allows

Table 2. **Shape generation.** We compute the Minimum Matching Distance MMD ($\times 10^4$) and Coverage Score (COV) (%), using the Chamfer Distance (CD), between generated and test shapes.

	MMD-CD (\downarrow)			COV-CD (% , \uparrow)		
	Car	Mixer	Chair	Car	Mixer	Chair
3DS2VS	21.43	14.26	55.99	80.48	31.28	89.51
PQ-NET	30.61	25.25	70.68	43.81	50.26	74.91
Ours	20.67	11.97	55.16	85.71	86.67	85.77

us to accurately recover shapes and their parts, even though the thin structures of the mixers are more challenging.

4.2. Shape Generation

We compare PartSDF’s shape generation abilities against those of 3DShape2VecSet and PQ-NET. The former relies on a diffusion model and the latter on a latentGAN (Achliopotas et al., 2018) to yield latent vectors from which shape or parts are decoded. For PartSDF, we leverage SALAD (Koo et al., 2023), a cascaded diffusion model that first generates part poses and then part latents conditioned on these poses. This also enables us to generate shapes fitting specified pose decompositions, something that PQ-NET cannot do with its single latent space. We report MMD and COV metrics in Table 2 and show generated examples in Figure 5. PartSDF achieves consistently better results than PQ-NET, with more detailed composite shapes. Our results are also better than, or on-par with, those 3DShape2VecSet, with the added bonus that our models are part-aware whereas those of 3DShape2VecSet are not, and therefore not usable for engineering design. Furthermore, it requires training different models for shape reconstruction and generation, while we use only one for both.

4.3. Part Manipulation

We evaluate our model’s ability to perform part-specific shape manipulation by editing part latent vectors and poses in Figure 6. Both latents and poses can be edited conjointly in PartSDF, we do so separately here for visualization purposes. When modifying part latents, the appearance of the corresponding parts is changed but the shape’s structure and parts layout remain fixed. On the other hand, when changing poses, the parts layout adapts and their general appearance is unchanged. In all cases, the resulting composite shape preserves its overall consistency while fitting the editions. These qualitative results emphasize the flexibility of our part-based representation, showing that our model can adapt individual parts independently while preserving overall shape integrity.

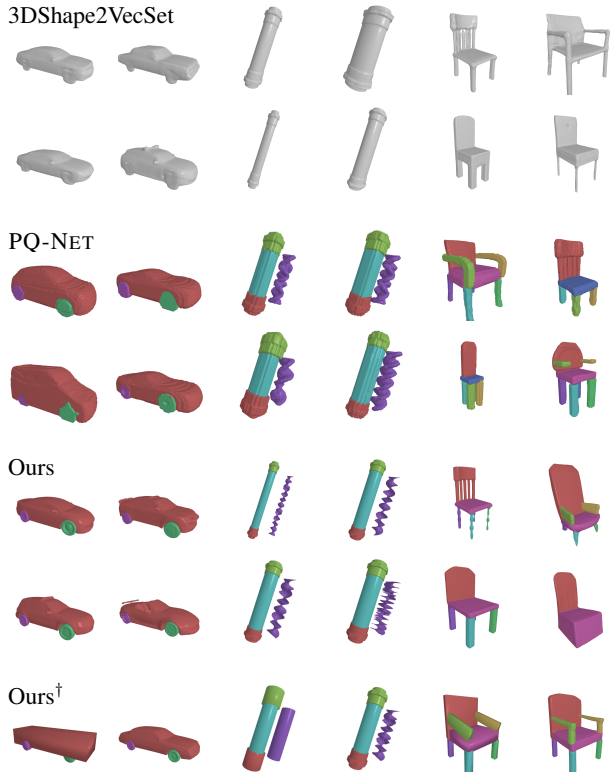


Figure 5. **Shape generation.** We generate shapes on all datasets and we also provide examples of pose conditioned generation (Ours[†]) where part latents are generated based on the poses’ coarse description of the shape (left image for each pair). We translate the helix outside of the mixer for visualization.

4.4. Part Optimization

To demonstrate the effectiveness of PartSDF as a part-aware shape prior for downstream tasks, we address a key engineering problem: Refining the shape of a car to reduce the drag induced by air flowing over its surface \mathcal{S} , *without* editing the wheels. Drag can be computed as the surface integral of the air pressure

$$\text{drag}_p(\mathcal{S}) = \iint_{\mathcal{S}} -n_x(\mathbf{x}) \cdot p(\mathbf{x}) d\mathcal{S}(\mathbf{x}), \quad (9)$$

where $p(\mathbf{x})$ is the pressure and $\mathbf{n}(\mathbf{x})$ the surface normal at point \mathbf{x} , with n_x its component along the x axis, which is directed along the car from front to back. This value is then normalized to get the drag coefficient C_d (Munson et al., 2013). For simplicity, we ignore the *friction* drag that tends to be negligible for cars. To compute a *differentiable* estimate of the surface pressure $\hat{p}(\mathbf{x})$ and resulting drag, we use a GCNN surrogate model (Baque et al., 2018). More specifically, we use a GraphSage Convolution GNN (Hamilton et al., 2017; Bonnet et al., 2022) to predict $\hat{p}(\mathbf{x})$ on the mesh’s surface, using simulation data obtained with OpenFOAM (OpenCFD).

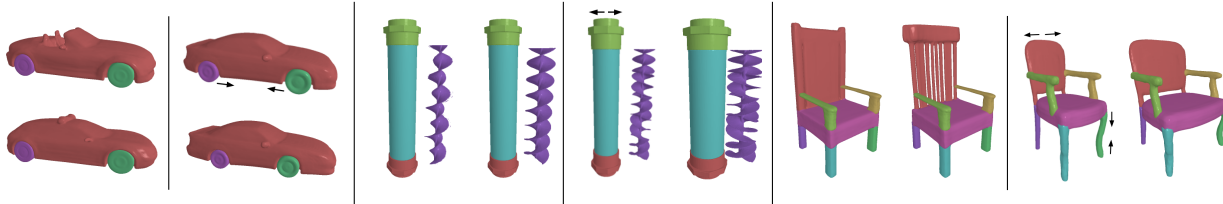


Figure 6. Shape manipulation. We manipulate two shapes per dataset, first by changing the latent of specific parts (car body, mixer helix, and chair backrest) and second by editing part poses (car wheels, mixer width, chair width and height). In all cases, the parts adapts to the modifications and to each other, maintaining a coherent whole with the new parts.

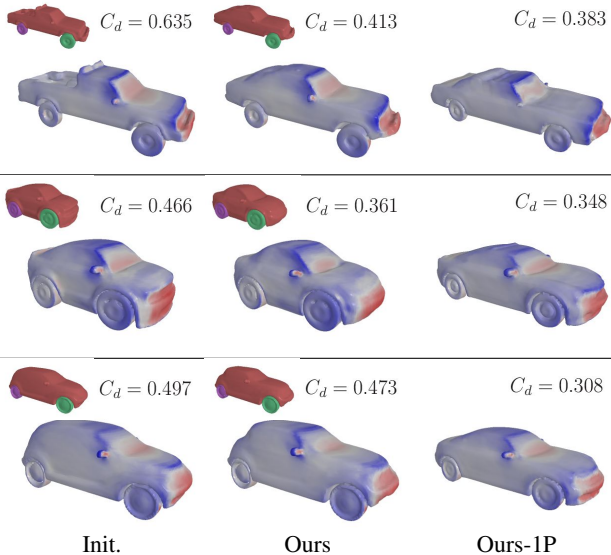


Figure 7. Part Optimization. (Init.) Initial shape. (Ours) Car body optimized to reduce aerodynamic drag with unchanged wheels. Our part-based representation enables this. (Ours-IP) When using a part-agnostic approach, everything changes, including the wheels. We highlight individual parts in the insert, give the drag coefficient C_d , and show the surface pressures (from blue to red).

Shape optimization can then be achieved by minimizing

$$\begin{aligned} \mathcal{L}_{\text{drag}} &= C_d(\mathcal{S}) + \mathcal{L}_{\text{reg}}(\mathbf{Z}, \mathbf{P}), \\ \mathcal{S} &= \text{MC}(f_{\theta}, \mathbf{Z}, \mathbf{P}), \end{aligned} \quad (10)$$

with respect to (\mathbf{Z}, \mathbf{P}) , where \mathcal{L}_{reg} are optional regularization terms and MC is the Marching Cubes algorithm (Lewiner et al., 2003). Importantly, gradients can be computed through the meshing step (Remelli et al., 2020). In practice, we minimize $\mathcal{L}_{\text{drag}}$ over the PartSDF latents \mathbf{Z} and pose parameters \mathbf{P} , starting from their values for an existing car. In the example of Fig. 7, we optimize the shapes of several cars while keeping their wheels unchanged, which is something that our part-based approach allows and can not be done with a global representation such as the one of Ours-1P or 3DShape2VecSet (Zhang et al., 2023). While they may achieve lower final drag, the shapes don’t respect design constraints, which is undesirable. For instance, in the second and last row of Figure 7, results with Ours-1P tend to converge to an average car, ignoring the specificity

of the initial cars and their wheels. We provide more details and results in Appendix C.

5. Limitations

The main limitation of PartSDF is its reliance on part labels during training. For our intended application, computer-aided design, this is not a major issue because the decomposition of shapes into parts is known *a priori*. Thus PartSDF is particularly relevant in scenarios where objects are naturally created with part-aware structures. While this limits PartSDF’s applicability to datasets without predefined decompositions—such as most of those available online—it better matches with practical engineering requirements. Nonetheless, if generalization to unlabeled data is desired, PartSDF could be combined with co-segmentation methods to generate pseudo-labels for its training.

6. Conclusion

In this work, we introduced PartSDF, a modular and supervised approach specifically designed for composite shape representation. PartSDF enables flexible, part-based shape modeling, supporting independent part manipulation and optimization while maintaining overall shape coherence. Our method leverages a simple architecture, achieving strong performance across tasks such as shape reconstruction, manipulation and generation.

Experimental results demonstrate that PartSDF consistently outperforms baseline methods in part-level accuracy, and can be adapted to a wide range of tasks, highlighting its effectiveness as a robust shape prior for composite structures. This flexibility makes PartSDF particularly suited for applications in fields like engineering design, where precise control over individual components is essential for customization and optimization.

While PartSDF achieves promising results, future work will explore enhancing part interactions to further support applications involving highly dynamic shapes or complex inter-part dependencies. Furthermore, developing more advanced topological supervision for each part should also be investigated to help prevent topologically inconsistent predictions, further improving its the robustness and applicability.

Impact Statement

This paper presents work whose goal is to advance the fields of Machine Learning and Computer-Aided Design. There are many potential societal consequences of our work, none which we feel must be specifically highlighted here.

References

- Achlioptas, P., Diamanti, O., Mitliagkas, I., and Guibas, L. Learning Representations and Generative Models for 3D Point Clouds. In *International Conference on Machine Learning*, pp. 40–49, 2018.
- Allaire, G. A Review of Adjoint Methods for Sensitivity Analysis, Uncertainty Quantification and Optimization in Numerical Codes. *Ingénieurs de l’Automobile*, 836: 33–36, July 2015.
- Atzmon, M. and Lipman, Y. SAL: Sign Agnostic Learning of Shapes from Raw Data. In *Conference on Computer Vision and Pattern Recognition*, 2020.
- Baqué, P., Remelli, E., Fleuret, F., and Fua, P. Geodesic Convolutional Shape Optimization. In *International Conference on Machine Learning*, 2018.
- Bonnet, F., Mazari, J. A., Cinnella, P., and Gallinari, P. AirFRANS: High Fidelity Computational Fluid Dynamics Dataset for Approximating Reynolds-Averaged Navier–Stokes Solutions. In *Advances in Neural Information Processing Systems*, 2022. URL <https://arxiv.org/abs/2212.07564>.
- Chang, A., Funkhouser, T., G., L., Hanrahan, P., Huang, Q., Li, Z., Savarese, S., Savva, M., Song, S., Su, H., Xiao, J., Yi, L., and Yu, F. Shapenet: An Information-Rich 3D Model Repository. In *arXiv Preprint*, 2015.
- Chen, Z. and Zhang, H. Learning Implicit Fields for Generative Shape Modeling. In *Conference on Computer Vision and Pattern Recognition*, 2019.
- Chen, Z., Yin, K., Fisher, M., Chaudhuri, S., and Zhang, H. BAE-NET: Branched Autoencoder for Shape Co-Segmentation. *International Conference on Computer Vision*, 2019.
- Chen, Z., Chen, Q., Zhou, H., and Zhang, H. DAE-Net: Deforming Auto-Encoder for fine-grained shape co-segmentation. *ACM SIGGRAPH*, 2023.
- Cho, K., Merriënboer, B. V., Gulcehre, C., Bahdanau, D., Bougares, F., Schwenk, H., and Bengio, Y. Learning Phrase Representations Using RNN Encoder-Decoder for Statistical Machine Translation. In *arXiv Preprint*, 2014.
- Choy, C., Xu, D., Gwak, J., Chen, K., and Savarese, S. 3D-R2n2: A Unified Approach for Single and Multi-View 3D Object Reconstruction. In *European Conference on Computer Vision*, pp. 628–644, 2016.
- Dai, A., Qi, C., and Nießner, M. Shape Completion Using 3D-Encoder-Predictor CNNs and Shape Synthesis. In *Conference on Computer Vision and Pattern Recognition*, 2017.
- Deng, B., Genova, K., Yazdani, S., Bouaziz, S., Hinton, G., and Tagliasacchi, A. Cvxnet: Learnable Convex Decomposition. In *Conference on Computer Vision and Pattern Recognition*, pp. 31–44, 2020.
- Deng, B., Kulal, S., Deng, Z., Deng, C., Tian, Y., and Wu, J. Unsupervised Learning of Shape Programs with Repeatable Implicit Parts. In *Advances in Neural Information Processing Systems*, 2022.
- Dupont, E., Kim, H., Eslami, S. M. A., Rezende, D. J., and Rosenbaum, D. From data to functa: Your data point is a function and you can treat it like one. In *International Conference on Machine Learning*, 2022.
- Fan, H., Su, H., and Guibas, L. A Point Set Generation Network for 3D Object Reconstruction from a Single Image. In *Conference on Computer Vision and Pattern Recognition*, 2017.
- Genova, K., Cole, F., Vlastic, D., Sarna, A., Freeman, W. T., and Funkhouser, T. Learning Shape Templates with Structured Implicit Functions. In *International Conference on Computer Vision*, pp. 7154–7164, 2019.
- Goodfellow, I., Pouget-Abadie, J., Mirza, M., Xu, B., Warde-Farley, D., Ozair, S., Courville, A., and Bengio, Y. Generative Adversarial Nets. In *Advances in Neural Information Processing Systems*, 2014.
- Gropp, A., Yariv, L., Haim, N., Atzmon, M., and Lipman, Y. Implicit Geometric Regularization for Learning Shapes. In *International Conference on Machine Learning*, 2020.
- Groueix, T., Fisher, M., Kim, V., Russell, B., and Aubry, M. Atlasnet: A Papier-Mâché Approach to Learning 3D Surface Generation. In *Conference on Computer Vision and Pattern Recognition*, 2018.
- Guillard, B., Stella, F., and Fua, P. MeshUDF: Fast and Differentiable Meshing of Unsigned Distance Field Networks. In *European Conference on Computer Vision*, pp. 576–592, 2022.
- Guillard, B., Remelli, E., Lukoianov, A., Richter, S., Bagautdinov, T., Baque, P., and Fua, P. DeepMesh: Differentiable Iso-Surface Extraction. *IEEE Transactions on Pattern Analysis and Machine Intelligence*, 2024.

- Hamilton, W. L., Ying, R., and Leskovec, J. Inductive representation learning on large graphs. In *Proceedings of the 31st International Conference on Neural Information Processing Systems*, 2017.
- Hao, Z., Averbuch-Elor, H., Snavely, N., and Belongie, S. Dualsdf: Semantic Shape Manipulation Using a Two-Level Representation. In *Conference on Computer Vision and Pattern Recognition*, pp. 7631–7641, 2020.
- Ho, J., Jain, A., and Abbeel, P. Denoising diffusion probabilistic models. In *Advances in Neural Information Processing Systems*, 2020.
- Hui, K.-H., Li, R., Hu, J., and Fu, C.-W. Neural Template: Topology-aware Reconstruction and Disentangled Generation of 3D Meshes. In *Conference on Computer Vision and Pattern Recognition*, 2022.
- Jacobson, A., Panozzo, D., et al. libigl: A Simple C++ Geometry Processing Library, 2018. <https://libigl.github.io/>.
- Ju, T., Losasso, F., Schaefer, S., and Warren, J. Dual Contouring of Hermite Data. In *ACM SIGGRAPH*, 2002.
- Kanazawa, A., Tulsiani, S., Efros, A., and Malik, J. Learning Category-Specific Mesh Reconstruction from Image Collections. In *Conference on Computer Vision and Pattern Recognition*, 2018.
- Kingma, D. P. and Ba, J. Adam: A Method for Stochastic Optimisation. In *International Conference on Learning Representations*, 2015.
- Kluger, F., Ackermann, H., Brachmann, E., Yang, M., and Rosenhahn, B. Cuboids Revisited: Learning Robust 3D Shape Fitting to Single RGB Images. In *Conference on Computer Vision and Pattern Recognition*, pp. 13070–13079, 2021.
- Koo, J., Yoo, S., Nguyen, M. H., and Sung, M. SALAD: Part-level latent diffusion for 3d shape generation and manipulation. In *International Conference on Computer Vision*, 2023.
- Lewiner, T., Lopes, H., Vieira, A. W., and Tavares, G. Efficient Implementation of Marching Cubes’ Cases with Topological Guarantees. In *Journal of Graphics Tools*, 2003.
- Li, S., Paschalidou, D., and Guibas, L. PASTA: Controllable Part-Aware Shape Generation with Autoregressive Transformers. In *arXiv Preprint*, 2024.
- Lorensen, W. and Cline, H. Marching Cubes: A High Resolution 3D Surface Construction Algorithm. In *ACM SIGGRAPH*, pp. 163–169, 1987.
- Mescheder, L., Oechsle, M., Niemeyer, M., Nowozin, S., and Geiger, A. Occupancy Networks: Learning 3D Reconstruction in Function Space. In *Conference on Computer Vision and Pattern Recognition*, pp. 4460–4470, 2019.
- Mo, K., X., S. Z. A., Chang, Yi, L., Tripathi, S., Guibas, L. J., and Su, H. PartNet: A large-scale benchmark for fine-grained and hierarchical part-level 3D object understanding. In *Conference on Computer Vision and Pattern Recognition*, 2019.
- Munson, B., Okiishi, T., Huebsch, W., and Rothmayer, A. *Fluid Mechanics*. Wiley Singapore, 2013.
- Niu, C., Li, J., and Xu, K. Im2struct: Recovering 3D Shape Structure from a Single Rgb Image. In *Conference on Computer Vision and Pattern Recognition*, pp. 4521–4529, 2018.
- O., A. H., Perel, Giryas, R., Sorkine-Hornung, O., and Cohen-Or, D. SPAGHETTI: Editing implicit shapes through part aware generation. *ACM Transactions on Graphics*, 2022.
- OpenCFD, L. OpenFoam. <https://www.openfoam.com/>.
- Pan, J. and Jia, K. Deep Mesh Reconstruction from Single RGB Images via Topology Modification Networks. In *International Conference on Computer Vision*, 2019.
- Park, J. J., Florence, P., Straub, J., Newcombe, R. A., and Lovegrove, S. Deepsdf: Learning Continuous Signed Distance Functions for Shape Representation. In *Conference on Computer Vision and Pattern Recognition*, 2019.
- Pascanu, R., Mikolov, T., and Bengio, Y. On the Difficulty of Training Recurrent Neural Networks. In *International Conference on Machine Learning*, pp. 1310–1318, 2013.
- Paschalidou, D., Ulusoy, A. O., and Geiger, A. Superquadrics Revisited: Learning 3D Shape Parsing Beyond Cuboids. In *Conference on Computer Vision and Pattern Recognition*, pp. 10344–10353, 2019.
- Paschalidou, D., Gool, L. V., and Geiger, A. Learning Unsupervised Hierarchical Part Decomposition of 3D Objects from a Single Rgb Image. In *Conference on Computer Vision and Pattern Recognition*, pp. 1060–1070, 2020.
- Paschalidou, D., Katharopoulos, A., Geiger, A., and Fidler, S. Neural Parts: Learning Expressive 3D Shape Abstractions with Invertible Neural Networks. In *Conference on Computer Vision and Pattern Recognition*, pp. 3204–3215, 2021.
- Paszke, A., Gross, S., Chintala, S., Chanan, G., Yang, E., Devito, Z., Lin, Z., Desmaison, A., Antiga, L., and Lerer,

- A. Automatic Differentiation in Pytorch. In *Advances in Neural Information Processing Systems*, 2017.
- Peng, S., Niemeyer, M., Mescheder, L., Pollefeys, M., and Geiger, A. Convolutional Occupancy Networks. In *European Conference on Computer Vision*, pp. 523–540, 2020.
- Peng, S., Jiang, C., Liao, Y., Niemeyer, M., Pollefeys, M., and Geiger, A. Shape as Points: A Differentiable Poisson Solver. In *Advances in Neural Information Processing Systems*, 2021.
- Petrov, D., Gadelha, M., Měch, R., and Kalogerakis, E. ANISE: Assembly-based Neural Implicit Surface rEconstruction. In *IEEE Transactions on Visualization and Computer Graphics*, 2023.
- Piegl, L. On NURBS: A Survey. *Computer Graphics and Applications*, 11:55–71, 1991.
- Remelli, E., Lukoianov, A., Richter, S., Guillard, B., Bagautdinov, T., Baque, P., and Fua, P. Meshsdf: Differentiable Iso-Surface Extraction. In *Advances in Neural Information Processing Systems*, 2020.
- Riegler, G., Ulusoy, A. O., and Geiger, A. Octnet: Learning Deep 3D Representations at High Resolutions. In *Conference on Computer Vision and Pattern Recognition*, 2017.
- Salimans, T. and Kingma, D. Weight Normalization - A Simple Reparameterization to Accelerate Training of Deep Neural Networks. In *Advances in Neural Information Processing Systems*, 2016.
- Shuai, Q., Zhang, C., Yang, K., and Chen, X. DPF-Net: Combining Explicit Shape Priors in Deformable Primitive Field for Unsupervised Structural Reconstruction of 3D Objects. In *International Conference on Computer Vision*, 2023.
- Sitzmann, V., Martel, J., Bergman, A., Lindell, D., and Wetzstein, G. Implicit Neural Representations with Periodic Activation Functions. In *Advances in Neural Information Processing Systems*, 2020.
- Smirnov, D., Fisher, M., Kim, V. G., Zhang, R., and Solomon, J. Deep Parametric Shape Predictions Using Distance Fields. In *Conference on Computer Vision and Pattern Recognition*, 2020.
- Sohl-Dickstein, J., Weiss, E. A., Maheswaranathan, N., and Ganguli, S. Deep unsupervised learning using nonequilibrium thermodynamics. In *International Conference on Machine Learning*, 2015.
- Stutz, D. and A.Geiger. Learning 3D Shape Completion from Laser Scan Data with Weak Supervision. In *Conference on Computer Vision and Pattern Recognition*, 2018.
- Sun, C., Zou, Q., Tong, X., and Liu, Y. Learning Adaptive Hierarchical Cuboid Abstractions of 3D Shape Collections. *ACM Transactions on Graphics*, 38(6):1–13, 2019.
- Takikawa, T., Litalien, J., Yin, K., Kreis, K., Loop, C., Nowrouzezahrai, D., Jacobson, A., McGuire, M., and Fidler, S. Neural Geometric Level of Detail: Real-time Rendering with Implicit 3D Shapes. In *Conference on Computer Vision and Pattern Recognition*, 2021.
- Tatarchenko, M., Dosovitskiy, A., and Brox, T. Octree Generating Networks: Efficient Convolutional Architectures for High-Resolution 3D Outputs. In *International Conference on Computer Vision*, 2017.
- Tulsiani, S., Su, H., Guibas, L. J., Efros, A. A., and Malik, J. Learning Shape Abstractions by Assembling Volumetric Primitives. In *Conference on Computer Vision and Pattern Recognition*, pp. 2635–2643, 2017.
- Vasu, S., Talabot, N., Lukoianov, A., Baque, P., Donier, J., and Fua, P. HybridSdf: Combining Free Form Shapes and Geometric Primitives for Effective Shape Manipulation. In *International Conference on 3D Vision*, 2022.
- Vaswani, A., Shazeer, N., Parmar, N., Uszkoreit, J., Jones, L., Gomez, A. N., Kaiser, L., and Polosukhin, I. Attention is All You Need. In *Advances in Neural Information Processing Systems*, 2017.
- Wang, N., Zhang, Y., Li, Z., Fu, Y., Liu, W., and Jiang, Y. Pixel2mesh: Generating 3D Mesh Models from Single RGB Images. In *European Conference on Computer Vision*, 2018.
- Wang, P.-S., Liu, Y., and Tong, X. Dual Octree Graph Networks for Learning Adaptive Volumetric Shape Representations. In *ACM SIGGRAPH*, volume 41, 2022.
- Wieser, D., Schmidt, H.-J., Müller, S., Strangfeld, C., Nayeri, C., and Paschereit, C. Experimental Comparison of the Aerodynamic Behavior of Fastback and Notchback DrivAer Models. *SAE Int. J. Passeng. Cars - Mech. Syst.*, 7(2):682–691, November 2014.
- Wu, J., Zhang, C., Xue, T., Freeman, B., and Tenenbaum, J. Learning a Probabilistic Latent Space of Object Shapes via 3D Generative-Adversarial Modeling. In *Advances in Neural Information Processing Systems*, pp. 82–90, 2016.
- Wu, R., Zhuang, Y., Xu, K., Zhang, H., and Chen, B. PQ-NET: A Generative Part Seq2Seq Network for 3D Shapes. In *Conference on Computer Vision and Pattern Recognition*, 2020.

- Wu, Z., Song, S., Khosla, A., Yu, F., Zhang, L., Tang, X., and Xiao, J. 3D Shapenets: A Deep Representation for Volumetric Shapes. In *Conference on Computer Vision and Pattern Recognition*, pp. 1912–1920, 2015.
- Xu, Q., Wang, W., Ceylan, D., Mech, R., and Neumann, U. DISN: Deep Implicit Surface Network for High-Quality Single-View 3D Reconstruction. In *Advances in Neural Information Processing Systems*, 2019.
- Yang, K. and Chen, X. Unsupervised Learning for Cuboid Shape Abstraction via Joint Segmentation from Point Clouds. In *ACM Transactions on Graphics (TOG)*, 2021.
- Yang, Y., Feng, C., Shen, Y., and Tian, D. Foldingnet: Point Cloud Auto-Encoder via Deep Grid Deformation. In *Conference on Computer Vision and Pattern Recognition*, June 2018.
- Zeng, X., Vahdat, A., Williams, F., Gojcic, Z., Litany, O., Fidler, S., and Kreis, K. LION: Latent Point Diffusion Models for 3D Shape Generation. In *Advances in Neural Information Processing Systems*, 2022.
- Zhang, B., Nießner, M., and Wonka, P. 3DILG: Irregular Latent Grids for 3D Generative Modeling. In *Advances in Neural Information Processing Systems*, 2022.
- Zhang, B., Tang, J., Nießner, M., and Wonka, P. 3DShape2VecSet: A 3D Shape Representation for Neural Fields and Generative Diffusion Models. In *ACM SIGGRAPH*, 2023.
- Zou, C., Yumer, E., Yang, J., Ceylan, D., and Hoiem, D. 3D-PRNN: Generating Shape Primitives with Recurrent Neural Networks. In *International Conference on Computer Vision*, 2017.

A. Table of Contents

In this supplementary material, we provide details regarding our implementation and experimental setup in Appendix B, explain the shape optimization experiment and give additional results in Appendix C, show parts interpolation in Appendix D, ablate components of PartSDF in Appendix E, and we provide additional experimental results in Appendix F: further visualizations for shape reconstruction (Appendix F.1), generation (Appendix F.2) and manipulation (Appendix F.3).

B. Implementation Details

In this section, we describe the architecture of PartSDF (Appendix B.1), its training procedure (Appendix B.2), and the point cloud encoder and diffusion models we used (Appendix B.3). Then, we detail our datasets and their processing (Appendix B.4), the baselines against which we compare and any hyperparameter choices (Appendix B.5), and finally the metrics used in this work and how they were computed (Appendix B.6).

B.1. Network Architecture

The final architecture of PartSDF, as presented in this work, is as follow:

The dimensionality of the part latent space is $Z = 256$, such that $\mathbf{z}_p \in \mathbb{R}^{256} \forall p$, and the hidden size of the fully-connected layers h_{fc} is 512, with the exception of the model trained on the *Chair* dataset where it is 256. This is because there are more parts, thus we expect each part to be simpler and it helps to alleviate the memory increase. We use weight normalization (Salimans & Kingma, 2016) on these layers, as in (Park et al., 2019). PartSDF has 8 h_{fc} layers, counting the input and output ones, with a convolutional layer h_{conv} between each pair, as described in Section 3.1. All layers, except the output one, are followed by ReLU non-linearities. See Figure 8 for a visualization of their arrangement in our decoder. Note that each h_{conv} has only $P^2 + P$ trainable parameters, e.g., $25 + 5 = 30$ parameters in the case of cars.

B.2. Training Procedure

The decoder model of PartSDF is trained for 2000 epochs using a batch size of 16 and 8192 sampled points per shape. We use the Adam optimizer (Kingma & Ba, 2015) with default parameters in PyTorch (Paszke et al., 2017), setting a learning rate of 5×10^{-4} for the model and 1×10^{-3} for the latent vectors. The learning rates are reduced by a factor of 0.35 at 80% and 90% of the total training epochs. The latent regularization weight is set to $\lambda = 10^{-4}$, and the non-intersection loss uses a softmax temperature parameter set to 0.02.

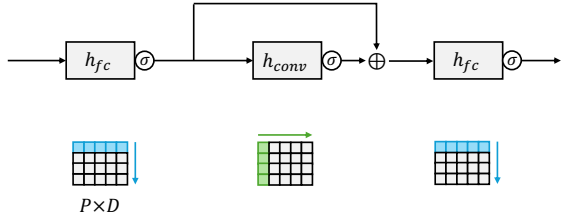


Figure 8. **Layer arrangement in PartSDF.** (Top) A convolutional layer h_{conv} is put between each pair of fully-connected layers h_{fc} , with an added residual connection, and every layer is followed by a non-linearity σ . (Bottom) For a given query position, the input tensor is of shape $P \times D$, with P the number of parts and D the feature size. h_{fc} operates on the D features for each part separately, while h_{conv} (with kernels of size 1) operates on the parts for each feature separately. The output is of shape $P \times D'$, with D' the output feature size of the second h_{fc} layer.

To supervise the SDF, we follow the sampling strategy used in DeepSDF (Park et al., 2019): 95% of the sampled points are near the surface, and 5% are uniformly distributed in space. The SDF values are computed using the IGL library (Jacobson et al., 2018), assuming watertight meshes. During training, the SDF values are clamped between -0.1 and 0.1 to focus the capacity of the network around the surface.

Trainings are conducted on a single NVIDIA V100 GPU with 32GB of memory, taking 1–2 days to train depending on the dataset size.

B.3. Encoder and Diffusion Models

Point Cloud Encoder. In Section 4.1, we use a point encoder to map point clouds of the full shapes to PartSDF parameter space, *i.e.* part latents and poses. For this, we leverage the model of 3DShape2VecSet (Zhang et al., 2023) using their official implementation¹. We use a smaller version of the model with 8 self-attention layers (against 24 in the original work), and without the final cross-attention layer with query positions (see Fig. 3 in their work) as we want to output part latents and poses instead of implicit values. We use learnable queries instead of point queries (see Fig. 4(a) in (Zhang et al., 2023)) to encode the point cloud, which creates an order on the latent set, allowing us to recover the parameters of specific parts. Note that we concatenate latent and pose for every part, such that the encoder outputs them both in a single vector.

Diffusion Model. In order to generate composite shapes with PartSDF, we use a diffusion model to generate the part latents and poses (Section 4.2), more specifically SALAD (Koo et al., 2023) with their official implemen-

¹<https://github.com/lzb/3DShape2VecSet>

tation². For the second diffusion on the latents, we however make use of a transformer decoder instead of encoder so that each part latent can attend to all part poses, and the part latents are normalized before training. This last point was found crucial for the diffusion as our latent vectors tend to have significantly lower norms than random vectors sampled from a multivariate Gaussian distribution. Indeed, as in (Park et al., 2019), latent vectors are initialized such that $\mathbb{E}_{\mathbf{z}_p} \|\mathbf{z}_p\| = 1$, while Gaussian noise in d -dimensions has $\mathbb{E}_{\mathbf{x} \sim \mathcal{N}^d} \|\mathbf{x}\| = \sqrt{d}$.

B.4. Datasets

For all datasets, we preprocess the meshes by centering them using their bounding box and rescaling them into the cube $[-0.9, 0.9]^3$, ensuring the longest edge of the bounding box measures 1.8. This leaves a margin around the shape to prevent the surface from leaving the meshing region, defined as the $[-1, 1]^3$ cube.

To create the SDF supervision, we perform two types of sampling (Park et al., 2019). First, we sample points on the surface of the mesh and perturb them with Gaussian noise, using variances of 0.005 and 0.0005 to generate points near the surface. Second, we uniformly sample points within the $[-1, 1]^3$ cube. The SDF values for all sampled points are computed using *libigl* (Jacobson et al., 2018). The samples and their SDF are mixed in a 95/5% ratio (near-surface to uniform samples) and stored for training. During training, a subset of these precomputed points is used, randomized at each epoch.

Additionally, each part, given as a subset of the original mesh, is fitted with a cuboid or cylinder. The orientation, translation, and scale of the primitive is then used as that part’s pose.

As explained in Section 4, obtaining high-quality composite shape data is challenging, with online data usually containing non-watertight meshes, or without part decomposition or an inconsistent one. Therefore, we use three curated datasets in this work.

Cars. In order to perform Computational Fluid Dynamics (CFD) simulations on the cars, see Appendix C below, we need them to be correctly closed and physically plausible, *i.e.* wheels and body correctly separated. We therefore hand-process a subset of ShapeNet (Chang et al., 2015)’s cars: The wheels and body are manually selected and separated, and then remeshed to become watertight (Wang et al., 2022).

Mixers. This dataset was proposed by (Vasu et al., 2022) and consists in liquid mixers made of a central tube, an

interior helix, and two attach points. It has the advantage of having an available, and consistent, part decomposition, which is suitable to learn a composite shape representation. The main challenge lies in the thinness of the tubes and helices, and the latter’s complexity.

Chairs. We use a clean subset of ShapeNet’s chairs with semantic segmentation provided by PartNet (Mo et al., 2019), with seat, backrest, armrest, and leg classes. To enable SDF computation, we first make the chairs watertight (Stutz & A.Geiger, 2018). Then, the PartNet segmentation, originally provided as a point cloud, is transferred to the mesh using a voting scheme: each face is assigned the most frequent class among its closest points. To refine this segmentation, we further divide the armrests and legs into individual parts by detecting connected components. Chairs that fail this finer segmentation are removed to ensure a consistency within our dataset. Additionally, we discard shapes at intermediate steps if they exhibit issues such as misalignment with the segmentation point cloud or a high Chamfer-Distance relative to the original shape.

Each dataset is split into train and test sets (80%/20%). Model hyperparameters are tuned using the train and validation sets, and final models, as reported below, are trained on train+validation and evaluated on the test set. Part poses are obtained by fitting each part with a cuboid or a cylinder.

B.5. Baselines

DAE-NET. DAE-NET (Chen et al., 2023) is a recent method that learns an unsupervised part decomposition to perform co-segmentation. It creates multiple part templates that are deformed to reconstruct a shape given its voxelization as input, allowing the original shape to be segmented based on the predicted decomposition. As mentioned in our main text, unsupervised methods like DAE-NET are typically designed to discover new shape decompositions, which is unsuitable for engineering design where parts have specific predefined meanings and uses. Additionally, as shown in our experiments, the reliance on voxelized inputs significantly limits its representation ability. We use the official implementation³ and conduct a grid search to tune the sparsity loss weight γ (see Eqs. (5) and (6) in their work). The optimal values found were $\gamma = 0.001$ for cars and mixers, and $\gamma = 0.002$ for chairs, consistent with their reported results.

BAE-NET. Similarly, BAE-NET (Chen et al., 2019) encodes a voxelized input to generate part implicit fields, which can be used for co-segmentation. The key difference, and the reason for comparison to our approach, is that BAE-NET also introduces a weak supervision scheme

²<https://github.com/KAIST-Visual-AI-Group/SALAD>

³<https://github.com/czq142857/DAE-Net>

where ground truth segmentations are provided for a small subset of the training shapes (typically ranging from 1 to 8 shapes). In this setting, the model propagates the learned decomposition across the entire dataset. Similar to DAE-NET, BAE-NET suffers from the limitations of voxelized inputs, which restrict its reconstruction accuracy. However, as shown in Figure 4, the weak supervision allows it to recover the desired decomposition in most cases, although certain parts, such as car wheels, are sometimes segmented together rather than individually. We use the official implementation⁴ to train the models. For the weak supervision, we experiment with 1, 2, 3, and 8 shots, finding that 8-shot supervision consistently yields the best results. Therefore, we use these models.

PQ-NET. As a fully supervised baseline, we compare against PQ-NET (Wu et al., 2020). PQ-NET employs a two-stage training process: first, an implicit auto-encoder is trained to reconstruct all individual parts, followed by a GRU-based RNN (Cho et al., 2014) that learns to auto-encode sequences of parts, represented by their latent vectors and bounding box parameters. For shape generation, latentGANs (Achlioptas et al., 2018) are used to sample in the RNN’s latent space. Like the previous baselines, PQ-NET relies on voxelized data and often reconstructs “inflated” shapes. While this helps against thinner parts, such as mixer helices and chair legs, the overall reconstruction accuracy remains low. Additionally, backpropagating through RNNs is notoriously difficult (Pascanu et al., 2013), and the non-continuous nature of its sequence generation makes it less suitable as a shape prior for optimization tasks. We train PQ-NET using the author’s official implementation⁵.

3DShape2VecSet. In order to evaluate the reconstruction and generation quality of our shapes against a more powerful baseline, we also compare to a state-of-the-art part-agnostic method, namely 3DShape2VecSet (Zhang et al., 2023). The core of the architecture is a large auto-encoder transformer (Vaswani et al., 2017) model that encodes a point cloud into an *unordered set* of latent vectors, which are then decoded at queried positions to obtain occupancy values. For generation, a KL-divergence loss is added during training to make the auto-encoder variational and help a second-stage diffusion model. This diffusion model is trained to generate *sets* of latent vectors, thus sampling 3DShape2VecSet’s latent space. As noted in the work, the models are very heavy, requiring multiple GPUs for training. Using the author’s official implementation⁶, we train auto-encoders *without* the KL-divergence loss for reconstruction experiments and *with* the KL-divergence for the genera-

tion experiments (as reference, we use the *same* PartSDF decoder for both experiments). We use the provided hyperparameters, except for the batch size that we limit to 256, from 512, because of memory constraints.

B.6. Metrics

Reconstruction. As we mention in the main text, to assess reconstruction accuracy of the 3D shapes, we use three metrics: For surface accuracy, we use the Chamfer-Distance (CD), which measures the *symmetric* distance between sets of points, $\mathcal{X} = \{\mathbf{x}_i\}_{i=1}^N$ and $\mathcal{Y} = \{\mathbf{y}_i\}_{i=1}^M$, sampled from the surface of the ground truth and reconstructed surfaces respectively. Their CD is then written

$$\text{CD}(\mathcal{X}, \mathcal{Y}) = \frac{1}{N} \sum_{\mathbf{x} \in \mathcal{X}} \min_{\mathbf{y} \in \mathcal{Y}} \|\mathbf{x} - \mathbf{y}\|^2 + \frac{1}{M} \sum_{\mathbf{y} \in \mathcal{Y}} \min_{\mathbf{x} \in \mathcal{X}} \|\mathbf{y} - \mathbf{x}\|^2. \quad (11)$$

In this work, we use $N = M = 30'000$, unless specified otherwise.

To evaluate the volume accuracy, we use Intersection over Union (IoU). It is defined as the ratio of volume between the intersection of the shapes over their union. In practice, we compute it using occupancy values on a grid: We find the smallest bounding box that contains the two shapes, then sample points on a 128^3 grid. For each point \mathbf{x} , we get the binary occupancy of each shape as $o_{S_1}(\mathbf{x})$ and $o_{S_2}(\mathbf{x})$, where $o_S(\mathbf{x})$ is 1 if \mathbf{x} is inside the shape and 0 otherwise. The IoU is then computed as

$$\text{IoU}(S_1, S_2) = \frac{\sum_{\mathbf{x}} o_{S_1}(\mathbf{x}) \cdot o_{S_2}(\mathbf{x})}{\sum_{\mathbf{x}} \max(1, o_{S_1}(\mathbf{x}) + o_{S_2}(\mathbf{x}))}. \quad (12)$$

Finally, we use Image Consistency (IC) (Guillard et al., 2022) to evaluate the appearance and surface normals, using renderings of the shapes. Let \mathcal{K} be a set of 8 cameras located at the vertices of a cuboid that encompasses the shape, looking at its centroid. For each camera $k \in \mathcal{K}$, we render the binary silhouettes $S_k \in \{0, 1\}^{256 \times 256}$ and normal map $N_k \in \mathbb{R}^{256 \times 256 \times 3}$ of shape S_1 , and similarly \tilde{S}_k and \tilde{N}_k for shape S_2 . The IC between these shapes is defined as

$$\text{IC}(S_1, S_2) = \frac{1}{|\mathcal{K}|} \sum_{k \in \mathcal{K}} \text{IoU}_{2D}(S_k, \tilde{S}_k) * \text{COS}(N_k, \tilde{N}_k), \quad (13)$$

where IoU_{2D} is the Intersection over Union between binary images and COS is the average cosine similarity between two normal maps. We refer interested readers to (Guillard et al., 2022) for more details.

We additionally report per-part average IoU (pIoU) as a way to measure part reconstruction accuracy, noting that CD and IC might have issues if the ground-truth parts are not watertight. In order to compute the occupancy of an open part,

⁴<https://github.com/czq142857/BAE-NET>

⁵<https://github.com/ChrisWu1997/PQ-NET>

⁶<https://github.com/lzb/3DShape2VecSet>

we rely on a strategy similar to our SDF supervision, see Figure 3. First, the occupancy of the full shape is computed on the grid. Then, for each point where the occupancy is 1, we look for the closest part to it. This part will get an occupancy of 1 at that point and all the others will get 0. Therefore, part occupancy can be seen as the intersection of the full shape’s occupancy with the part’s ”closest region” as visualized in Figure 3(b). Note that for baselines without part correspondences, *i.e.* DAE-NET and PQ-NET, we must first match the reconstructed parts to the ground truth (GT) ones: For each shape and each reconstructed part, we match it with the GT part with which it has the highest IoU.

Generation. To evaluate the plausibility and diversity of the generated shapes, as compared to a held out test set, we report the Minimum Matching Distance (MMD) and Coverage Score (COV) (Achlioptas et al., 2018) respectively, using the Chamfer-Distance as the (pseudo-)distance metric.

MMD is the average distance between each shape from the test set T and the generated set G . It is written as

$$\text{MMD}(G, T) = \frac{1}{|T|} \sum_{\mathcal{X} \in T} \min_{\mathcal{Y} \in G} \text{CD}(\mathcal{X}, \mathcal{Y}), \quad (14)$$

where we make the abuse of notation that $\text{CD}(\mathcal{X}, \mathcal{Y})$ means the Chamfer Distance between samples on the surfaces of \mathcal{X} and \mathcal{Y} .

On the other hand, COV measures the fraction of shapes in the test set that are recovered with a greedy matching of generated shapes: each shape in G is matched with the closest shape in T . Rigorously, it is computed as

$$\text{COV}(G, T) = \frac{|\{\arg \min_{\mathcal{X} \in T} \text{CD}(\mathcal{X}, \mathcal{Y}), \forall \mathcal{Y} \in G\}|}{|T|}. \quad (15)$$

For both the baseline and our method, we generate 2000 shapes, and use 2048 surface samples to compute the CD, for efficiency concern.

C. Part Optimization

As described in Section 4.4, we optimize shapes to demonstrate how PartSDF is used as a part-aware shape prior. In this section, we provide further experimental details and results.

Experimental Setup. The goal of this experiment is to optimize the shape of a car to minimize its aerodynamic drag, expressed as the drag coefficient (C_d), by modifying its main body under the constraints that wheels cannot be modified. Direct simulation of aerodynamic performance, such as Computational Fluid Dynamics (CFD) (OpenCFD), is computationally expensive and non-differentiable without

adjoint solvers (Allaire, 2015). To address this, we use a surrogate model to approximate drag-related metrics efficiently and differentially (Baqué et al., 2018; Remelli et al., 2020).

We use a graph convolutional neural network (GCNN), specifically with GraphSage layers (Hamilton et al., 2017), to predict the surface pressure distribution of a car. The predicted surface pressure is integrated to compute the drag force (Equation (9)), which is then normalized by the mass density of the fluid, its velocity squared, and the frontal surface area of the shape to obtain C_d . We simulate the cars in our dataset, following the well-established setup of the DrivAer model (Wieser et al., 2014), to compute the corresponding surface pressures and C_d values. The dataset thus created is used to trained the GCNN-based surrogate model.

Following this, all model parameters, those of PartSDF and the surrogate’s, are frozen for the shape optimization. It is performed by adjusting the latents \mathbf{Z} and/or poses \mathbf{P} of the parts, starting from the initial parametrization of an existing car. In this experiment, the wheels are kept fixed and only the body is optimized, which is only possible because of the composite shape representation of our model that also ensures coherence between the parts.

The optimization minimizes the integrated pressure drag predicted by the surrogate model, backpropagating through the meshing to adjust the part parameters (Equation (10)). Regularization terms \mathcal{L}_{reg} are applied to maintain consistency in the latent space and prevent excessive deviations:

- A k -nearest neighbors (kNN) loss on the latent vectors to ensure they remain close to the training distribution, as introduced in (Remelli et al., 2020), and
- an L_2 regularization on the deviation of latent vectors and poses from their initial values, *e.g.*, $\|\mathbf{Z} - \mathbf{Z}_{\text{init}}\|_2^2$.

To summarize, during a single iteration of this optimization process:

1. Current part latents and poses (\mathbf{Z}, \mathbf{P}) are used to compute the car’s SDF on a grid, as required by the Marching Cubes algorithm.
2. Marching Cubes is applied on the SDF grid to obtain a mesh of the car surface $\mathcal{S} = \text{MC}(f_\theta, \mathbf{Z}, \mathbf{P})$.
3. The mesh is passed through the GCNN surrogate to obtain the surface pressure $\hat{p}(\mathcal{S})$, from which the drag coefficient C_d is computed.
4. The gradient of $C_d + \mathcal{L}_{\text{reg}}$ is computed with respect to (\mathbf{Z}, \mathbf{P}), which are then updated through stochastic gradient descent.

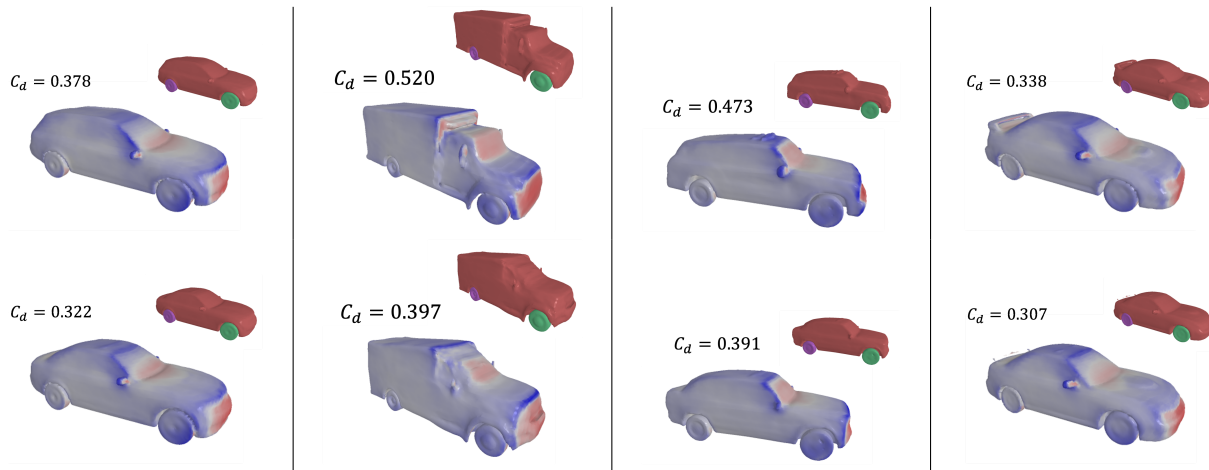


Figure 9. **Additional shape optimization.** The aerodynamic drag of the car is minimized with respect to the latent vector of the car’s body, with fixed wheels. We show the initial car pre-optimization (*top*) and the resulting car optimization (*bottom*), colored by surface pressure from low to high pressure (blue to red). We also visualize the parts in the insert. We report the drag coefficient C_d before and after the shape optimization, as computed by a physical simulator (OpenCFD).

This setup allows us to efficiently optimize composite shapes for aerodynamic performance while leveraging the flexibility of PartSDF’s framework.

Results. With this experimental setup, we optimize multiple cars from our dataset and simulate the resulting shapes in OpenFOAM (OpenCFD) to obtain their final drag coefficient C_d . Because simulations are expensive ($> 10h$ depending on the meshing resolution of the 3D space), we must limit ourselves to a subset of 35 cars. The average drag coefficients before and after optimizations are

Before	After
0.378	0.325

with an average relative improvement of 12.7%. We visualize some optimization results in Figure 9. As can be observed, only the body of the car has been modified while the wheels are unchanged. Nonetheless, they stay consistent with each other and no inter-penetration happens.

D. Part Interpolation

To demonstrate the smoothness and consistency of our latent and pose space, we perform an interpolation experiment. Given pair of shapes, we linearly interpolate between their part latent vectors and poses, with the exception of rotation quaternions for which we use spherical linear interpolation (slerp). At multiple interpolation steps, we reconstruct the intermediate shapes using our decoder and visualize such interpolation “path” in Figure 10, illustrating smooth transitions between the pair of shapes. Notably, the part-

Table 3. **Ablation on PartSDF components.** We ablate the use of part poses, *latent modulation* (latMod) and convolutional layers (conv) on the Car dataset. Best performance is achieved with poses and latent modulation, though we note that convolutions decrease slightly the part accuracy of our model. However, this is counterbalanced by enabling part manipulation, as in Figure 11.

	CD (\downarrow)	IoU (% \uparrow)	IC (\uparrow)	pIoU (% \uparrow)
w/o poses	1.43	97.81	0.928	91.71
w/o latMod	1.39	97.37	0.923	92.33
w/o conv	1.27	98.02	0.932	96.37
PartSDF	1.27	98.02	0.931	94.89

based structure remains coherent throughout the interpolation. This highlights the effectiveness of our learned latent and pose spaces in representing composite shapes.

E. Ablation Study

We conduct an ablation study to evaluate the impact of convolutional layers, the use of pose parameters, and latent modulation in PartSDF, and report metrics on the Car dataset in Table 3. Pose parameters allow independent control of part transformations, which improves the shape reconstruction performance but also allows more precise part manipulation, while the addition of latent modulation is a simple modification that improves surface and part reconstruction, as measured by Chamfer-Distance and part IoU. On the other hand, convolutional layers cause a slight decrease in part accuracy, largely counterbalanced by the manipulation capability it enables. In Figure 11, we show that adding these layers to PartSDF maintains the consistency between parts

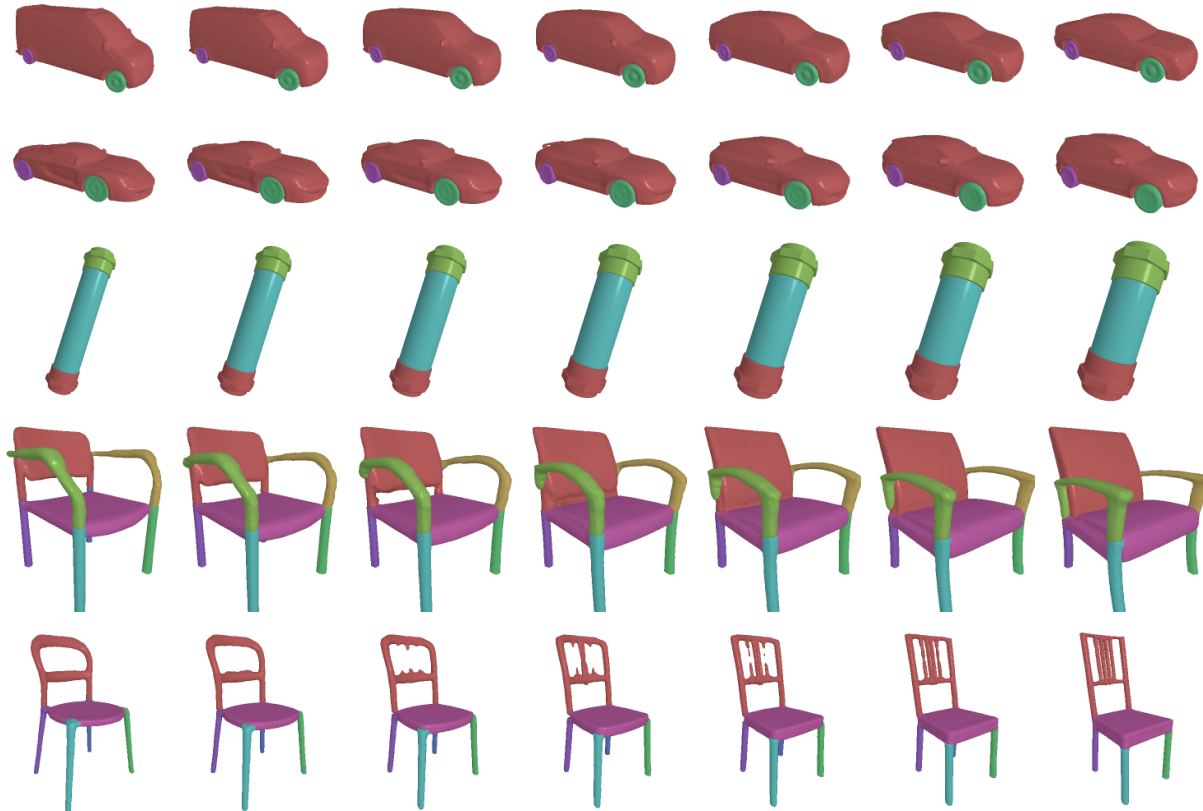


Figure 10. **Part interpolation.** On each row, we interpolate between the part latents and poses of one shape (*left*) to the other (*right*) and reconstruct the intermediate shapes. The overall shape structure is preserved while the parts change smoothly, remaining coherent with each others.

when doing part manipulation. Additionally, we show in Figure 11 the necessity of the non-intersection loss $\mathcal{L}_{\text{inter}}$: without it, the reconstruction losses do not prevent the parts from bleeding into one another, causing the model to learn an incorrect part decomposition with overlapping parts.

F. Additional Experimental Results

In this section, we provide additional results and visualization on shape reconstruction (Appendix F.1), generation (Appendix F.2) and manipulation (Appendix F.3).

F.1. Shape Reconstruction

We provide additional examples of shape reconstruction on the test set in Figure 12. We also visualize the part poses as primitives and results using the point encoder. DAE-NET and BAE-NET struggle to recover thin parts and complex shapes, while PQ-NET tend to inflates them without details. On the opposite, PartSDF recovers accurately the shapes and the parts. We note that with a point cloud encoder, the results may not be as accurate, *e.g.*, the last chair where the armrest segmentation is different, though it is still sensible.

F.2. Shape Generation

In Figure 13, we visualize generation examples with PQ-NET and PartSDF. We also show the part latent generation conditioned on poses for our model. The generated shapes with our method in combination of SALAD (Koo et al., 2023) are more detailed than PQ-NET + a latentGAN, with greater variety for cars and mixers (as reported in Table 2).

F.3. Shape Manipulation

Finally, we perform more manipulation in Figure 14 with PartSDF on all dataset. By changing part latents, the affected parts have modified appearances but adapt to the original pose and to each others. For example, the car bodies have the same general scales but their wheel wells fit correctly the original wheels, the mixers helices fit the original tube, and the chairs keep the same overall structure while each parts are locally different. When editing their poses, the parts are moved and deformed, but also preserve their original features, *e.g.*, the cars keep their original shapes but adapt to their new wheels, the mixers and their helices are rescaled but conserve their inside/outside relationship, and

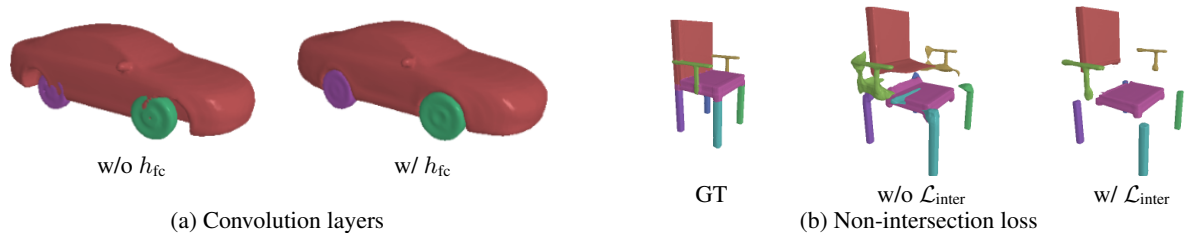


Figure 11. **Ablation study of PartSDF.** (a) Without the convolution layers h_{fc} (Section 3.1), manipulating a part does not affect the others: The translated and scaled wheels incorrectly collide with the car. With these added layers, manipulating some parts correctly affect the others: The car adapts to the new wheel poses without intersection. (b) Without the non-intersection loss \mathcal{L}_{inter} , the parts incorrectly overlaps. With it, the model learns the correct part decomposition.

the size and height of chairs can be changed while maintaining the chairs’ features. Note that this requires the part poses to be correct and coherent. Indeed, if they are manually set to be out of contact and disorganized in 3D space, the resulting shape will be meaningless.

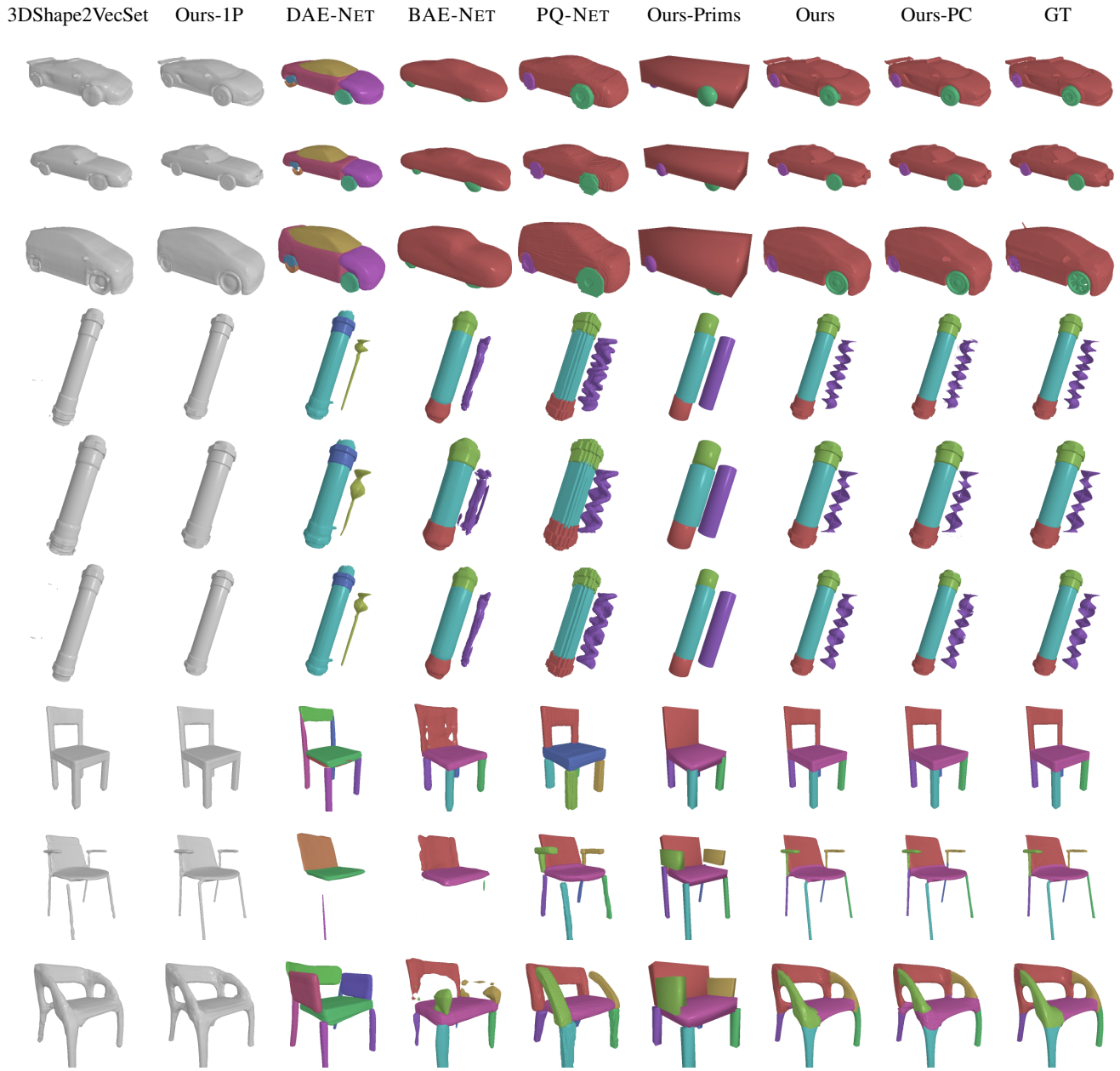


Figure 12. **Additional shape reconstruction.** Reconstructions of test shapes using either the baselines or our model. We use a single part with Ours-1P, we visualize the pose parts of Ours as cuboid or cylinders in Ours-Prims, and Ours-PC is the reconstruction using the point cloud encoder, as described in Section 4.1. For part-based method, we translate the helix outside of the mixers for visualization.

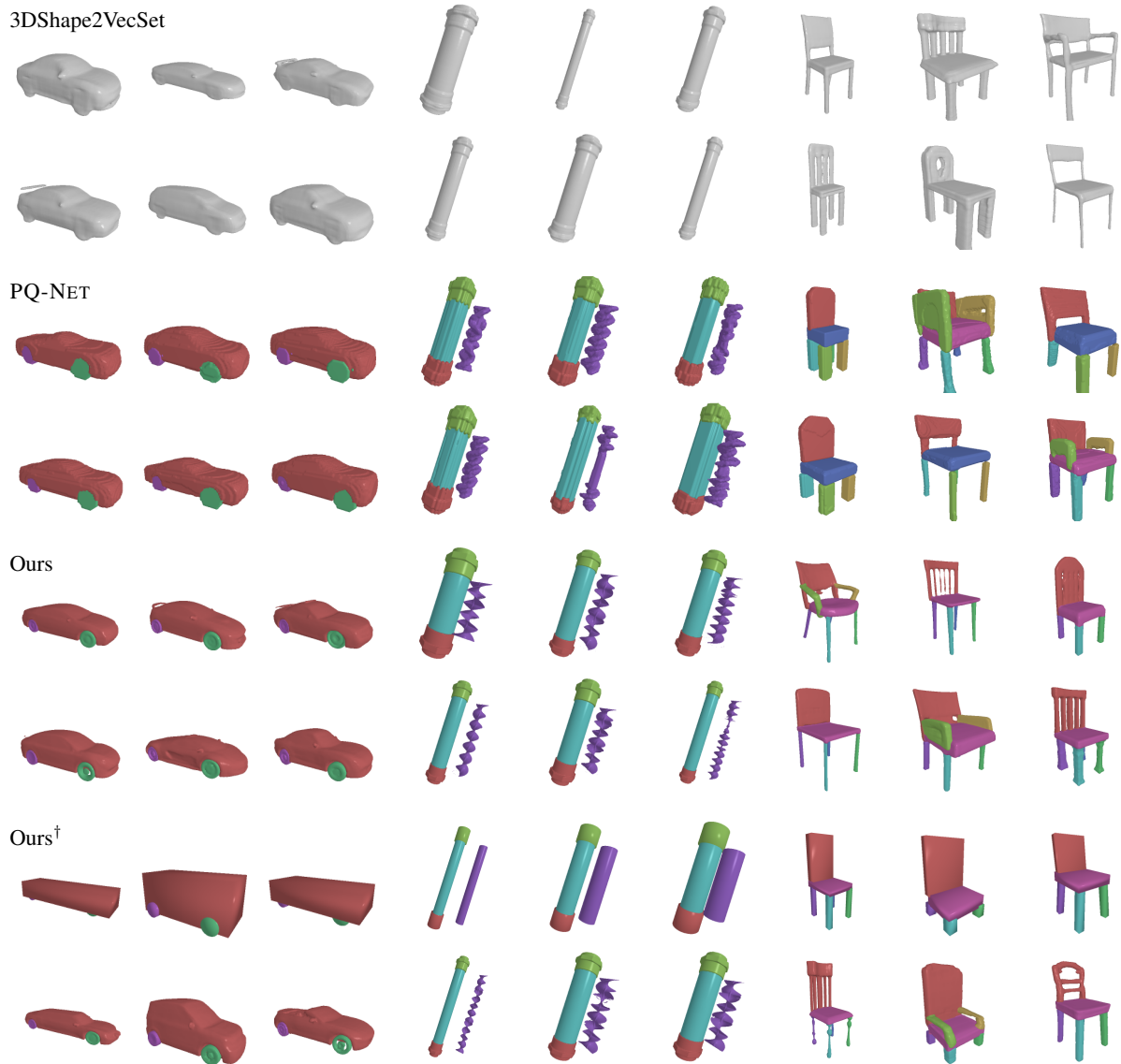


Figure 13. **Additional shape generation.** Randomly generated shapes and their parts on all datasets. We also provide examples of pose conditioned generation (Ours[†]) where part latents are generated based on the poses' coarse description of the shape (top image for each pair). The helix is translated outside of the mixers for visualization.

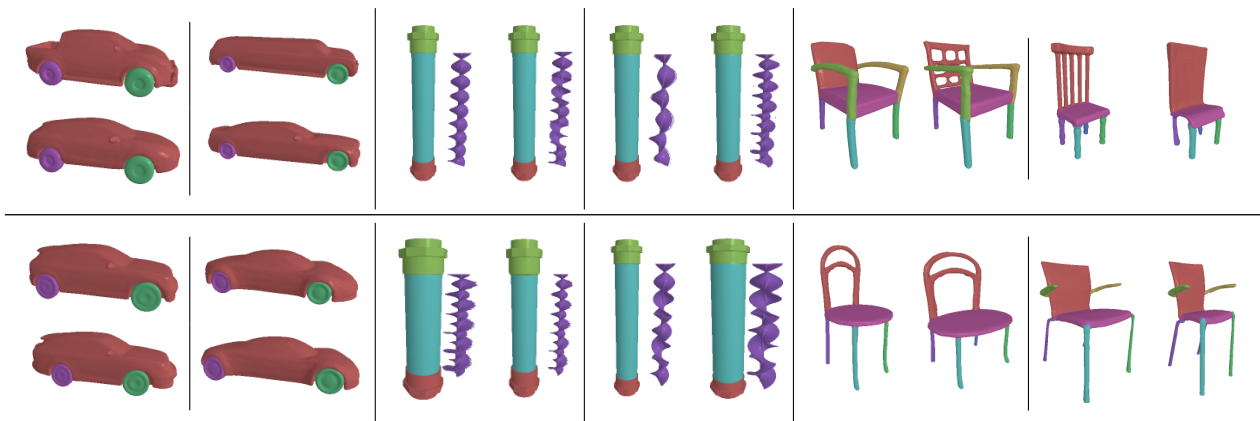


Figure 14. **Additional shape manipulation.** We manipulate four shapes per dataset: (*top*) by changing the latent of specific parts (car body, mixer helix, and all chair parts) and (*bottom*) by editing part poses (car wheels, mixer width, chair width and height). In all cases, the parts adapt to the modifications and to each other, maintaining a coherent whole.